Materials & Design 241 (2024) 112892

Contents lists available at ScienceDirect

Materials & Design

journal homepage: www.elsevier.com/locate/matdes

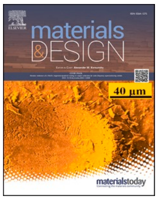

Decomposition and dewetting of super-saturated Cu-15 at. % Co solid solution film

Farnaz Farzam [a,*], Bárbara Bellón [a], Dominique Chatain [c], José A. Jiménez [d], Benjamin Breitbach [a], Matteo Ghidelli [a,b], María Jazmin Duarte [a], Gerhard Dehm [a,*]

[a] Max-Planck-Institut für Eisenforschung GmbH, Düsseldorf, Germany
[b] Laboratoire des Sciences des Procédés et des Matériaux (LSPM), CNRS, Université Sorbonne Paris Nord, Villetaneuse, France
[c] Aix-Marseille Univ, CNRS, CINaM, Marseille, France
[d] National Center for Metallurgical Research CENIM-CSIC, Av. De Gregorio del Amo 8, Madrid 28040, Spain

ARTICLE INFO

Keywords:
CoCu film
Thermal stability
Phase separation
Solid state dewetting

ABSTRACT

Nano-structured copper thin films present numerous applications for miniaturization of electronic devices. Their long term stability is key for reliable functionality. This work explores the thermal stability and solid state dewetting of a Cu-Co solid solution thin film and compares it to pure Cu. As according to the phase diagram Co is practically immiscible in Cu at room temperature, a metastable solid solution of Cu-15 at. % Co was deposited as thin film on a sapphire wafer. The microstructural evolution of the Co super-saturated film at temperatures ranging from 673 to 1073 K was evaluated using X-ray diffraction and high resolution microscopy techniques such as scanning electron and transmission electron microscopy. Interestingly, there is a competition between grain growth and phase separation. Co precipitates at grain boundaries acting as pinning sites preventing rapid grain growth during heat treatment at intermediate annealing temperature. However, grain growth occurs very quickly at higher temperatures, once the elemental phases of Cu and Co are formed. The competition between grain growth and phase separation and their consequence for dewetting are discussed.

1. Introduction

The importance of thin films in different technologies, from microelectronics with conductors and interconnects [1–6] to sensors [7] and magnetic recording media [8], has increased by daily emerging innovations in nanotechnology. By decreasing the size of devices, the thermal and mechanical stability of their components becomes more important.

The size-affected stability of thin films is a subject which has previously been widely studied [9–12]. For instance, there are studies about microstructural evolution and the dewetting of single element FCC metals [13,14], showing that 100 nm Ni films on sapphire are still intact after 1 h of annealing at ~ 50 % T_m (melting temperature) in an atmosphere of Ar and H_2 mixture. However, the grain size reached 2–5 times the film thickness after this time and further annealing at 873 K for another hour led to groove formation at the surface of the film [13]. In another study, the formation of holes was observed in a 100 nm thick polycrystalline Cu film at ~ 30 % T_m after three consecutive heat treatments with 10 min duration each [14]. What is commonly explained in all of these studies is that the solid state dewetting usually starts with grain growth followed by grain boundary grooving and hole formation at triple junctions [15], and finally leads to the formation of isolated particles. Moreover, the annealing atmosphere [16], temperature [16,17] and duration [17], as well as film thickness [13], can affect the dewetting behavior of the film in terms of morphological evolution and hole formation. However, very few studies have analyzed the effect of alloying on dewetting. Minamide *et al.* [18] found that the onset of dewetting in Ag films is delayed by adding Cu and Nb in different percentages. Each of these elements affected the dewetting behavior in a different way. Cu changed the Ag film texture and grain orientation evolution, while Nb oxides surrounded Ag grains and made the diffusion of Ag more sluggish [18]. Müller and Spolenak [19] have observed that the stability of Au films increased by adding less than 10 at. % Pt to the film. While there have been several studies on the alloying effect on dewetting of highly conductive elements such as Ag and Au, the exact mechanisms are not yet fully defined. One approach to address these mechanisms more precisely is to resolve the dewetting process of similar super-saturated alloy systems (CoCu in this study) with higher

---

* Corresponding authors.
E-mail addresses: far.farzam@gmail.com (F. Farzam), dehm@mpie.de (G. Dehm).

https://doi.org/10.1016/j.matdes.2024.112892
Received 2 February 2024; Received in revised form 28 March 2024; Accepted 29 March 2024

resolution. Moreover, investigating the thermal stability of more abundant yet highly conductive elements such as Cu can be useful for future applications. Therefore, in this study we explored the effect of alloying on solid-state dewetting of Cu films. We chose Co as the alloying element to avoid multiple phase transformations during heat treatments (see CoCu phase diagram in Ref. [20]). Thin films of Cu alloyed with magnetic elements such as Co have been the main focus of many studies. For example, Childress and Chien [21] studied the magnetic behavior of CoCu alloy films over a range of compositions. In addition, Mebed and Howe [22], as well as Hütten and Thomas [23] investigated the spinodal decomposition of CoCu thin films with different compositions and its correlation with giant magnetoresistance (GMR). In another study [24]. Mebed investigated the microstructural evolution and pointed to the dewetting of partially amorphous CoCu films during thermal annealing. However, the correlation between the decomposition process of a solid solution CoCu film and the solid state dewetting process has still remained unresolved. As these two phenomena, decomposition and dewetting, both occur as a result of temperature, a more in-depth study is needed to understand the sequence of the different mechanisms at play and their mutual effects.

Choosing Co in this study also provides a common ground, in terms of phase transformation, to discover stability of other compositions of CoCu films. On the other hand, we intended to keep the electrical conductivity of Cu unchanged during the annealing processes. So, we chose CoCu films with ~ 15 at. % Co to stay within the solid miscibility gap of the phase diagram [20], and applied high resolution techniques such as transmission electron microscopy (TEM) in parallel with scanning electron microscopy (SEM) and X-ray diffraction (XRD) in order to resolve how the introduction of a low amount of ~ 15 at. % Co into the Cu matrix affects morphological/ microstructural evolution and solid-state dewetting of Cu films. To complement previous studies on the CoCu system, we analyzed the onset temperatures of decomposition as well as the dewetting process. Moreover, we reveal how the phase separation leads to delay in dewetting of super-saturated CoCu films compared to pure Cu film resolving and understanding the competition phenomena between grain growth and precipitation.

2. Experimental procedures

CoCu films with elemental ratio of about 85/15 at. % were deposited on sapphire wafers by the physical vapor deposition (PVD) technique using a magnetron sputtering system (Bestec GmbH, Germany). For this purpose, standard 2-inch sapphire substrates, 0.33 ± 0.025 mm in thickness, epi-polished on one side (purchased from CrysTec Kristalltechnologie, Berlin, Germany) were used. These wafers have a maximum miscut of less than 0.1° from the $< 0001 >$ direction normal to the surface. The polished surface of the substrates was cleaned with a stream of nitrogen gas, and after this preparation, Co and Cu were co-sputtered to produce alloy films with the desired chemical composition. The purity of the metallic materials used for depositions was 99.95 and 99.999 % for the Co (EVOCHEM Advanced Material GmbH, Offenbach, Germany) and Cu (Kurt J. Lesker Company, England and Wales) targets, respectively. Depositions were carried out at room temperature using a background pressure of $\sim 10^{-6}$ Pa. The powers on the cathodes and the durations of deposition were chosen to reach Co-Cu films of about ~ 100 nm in thickness.

As-sputtered samples were cut into smaller pieces after deposition using a diamond tip (on the deposited side) to evaluate the effect of temperature on the solid-state dewetting process. These samples were annealed at different temperatures of 673, 773, 873, 973 and 1073 K for 4 h in a furnace equipped with an alumina tube. As the oxidation of the samples during heat treatment could greatly affect both, the surface diffusion and dewetting behavior, they were processed under a gas mixture of 91 vol% Argon (Ar) and 9 vol% H_2. After introducing the sample into the furnace, a continuous flow of Ar and H_2 of of 9.1 and 0.9 cc/min, respectively, was held for 1 h for purging the system of air. After the end of this cycle, the gas valves of the furnace were closed and the system was heated to the desired final temperature at a heating rate of 20 K/min. Furthermore, three larger samples (compatible with XRD measurements) were encapsulated in a quartz tube filled with similar composition of Ar and H_2. These samples were then annealed at 673, 873 and 1073 K and then quenched in air to room temperature.

The microstructure of an as-deposited as well as of the heat-treated samples was analyzed using a Rigaku SmartLab X-ray Diffractometer (XRD), and a Zeiss Sigma 500 Scanning Electron Microscope (SEM), a FEI Titan probe corrected (PC) Transmission Electron Microscope (TEM) equipped with bright field (BF), annular dark field (ADF) and high angle annular dark field (HAADF) detectors and a Jeol JEM-2100 TEM, all of them equipped with an energy dispersive X-ray spectrometer (EDS). The surface of the samples was coated with a thin layer of carbon (~2 nm) before introduction into the SEM to prevent charging. SEM images were used to analyze both, the surface morphology on an area of 23 × 17 μm and the thickness of the film cross sections at three different locations. Thickness measurements showed an average value of 98.1 ± 2.0 nm. This value is representative for the typical thickness of materials in nanotechnology applications. On the other hand, compositional homogeneity in both as-deposited and annealed samples was verified from EDS spectra recorded at 15 keV maintaining similar acquisition parameters (count rate, current, acquisition time and pixel size).

The phases present in the samples and their crystallographic texture were determined from the XRD measurement performed using a diffractometer equipped with a copper rotating anode ($\lambda\ K_{\alpha 1} = 0.15406$ nm), a Goebel mirror for parallel-beam geometry and an energy dispersive 2D detector. As films were sitting on a substrate, conventional θ–2θ scans were recorded in reflection mode over a 2θ range of 10-100° with a step size of 0.01° and scan speed of 2°/min over an area of 500 x 500 μm^2. The collected patterns were analyzed using the version 4.2 of Rietveld analysis program DIFFRACplus TOPAS (Bruker AXS GmbH, Karlsruhe, Germany) [25] and a structural model containing the crystallographic information of Cu and Co. These refinements included explicitly the lattice parameters of these two phases.

TEM images and corresponding EDS-maps with elemental distribution of Cu and Co were taken from the cross-sections of the as-deposited and annealed films. For these measurements, lamellas of about 100 nm thickness were prepared using a FEI-Scios2 focused-ion beam (FIB). First, ~8 nm carbon layer was added on the layer previously deposited for SEM-EDS measurements to avoid charging the surface and beam drift. Through all milling and thinning processes, a 30 kV Ga^+ beam was used. Prior to milling, a 500 nm Pt layer was deposited on the surface with the ion beam of 50 pA to protect the surface. This Pt layer was further increased to ~ 3 μm using 300 pA current. After the milling process, the ~ 1.5 μm thick lamella was transferred to the grid and thinned down to ~ 1 μm with an ion beam current of 1nA using the CCS (cleaning cross section) pattern. Further thinning to 500 and 200 nm was carried out using 300 and 100 pA currents, respectively. Last thinning step to 100 nm was done with 10 pA and finalized with a short thinning by 5 kV/ 7.7 pA ion beam.

The cross-sectional TEM images and their corresponding EDS elemental maps were acquired in a probe corrected Titan for the as-deposited film and heat-treated samples at 673 and 873 K, using 300 keV beam. Similar measurements for the film annealed at 1073 K were carried out in a Jeol JEM-2100 using a 200 keV beam.

The grain size characterization in the as-deposited and annealed films was carried out using cross-sectional TEM images. The length of the horizontal line passing through the center of 10 grains was measured for each TEM sample and the obtained average value was taken as representative of the whole sample.

3. Results and interpretation

High magnification SEM secondary electron (SE) images recorded from the as-deposited film show a nano-scale rough surface characterized by cells of about 20 nm in size, as displayed in Fig. 1a. The TEM cross-section image of Fig. 1b reveals that this cellular-like structure can be related with a microstructure consisting of nano-sized grains. This microstructure is characteristic of thin films deposited at temperature well lower than the melting point of the target materials, since under these conditions the thermally activated mobility processes are quite limited. Fig. 1a and b show also the absence of defects such as cracks or holes which may be key features for initiating dewetting. On the other hand, the TEM-EDS maps of the cross sections of the deposited film presented in Fig. 1c and d show a homogeneous solid solution phase and the absence of an oxide layer on the surface, respectively.

The average Co concentration of the films in as-deposited state and its evolution with the annealing temperature is shown in Fig. 2. Since the content of this element remains constant within the error bars of film composition in the as-deposited state at 14.8 ± 3.9 at. % Co, it was concluded that there is no loss of Co or Cu during the thermal treatments. Therefore, the changes in the surface morphology and microstructure of the films that could be observed in the annealed samples are not related to a compositional change of the film.

SE-SEM images of the film surface and the corresponding elemental concentration maps of Cu and Co are displayed in Fig. 3 for as-deposited film and after heat treatment at temperatures ranging from 673 to 1073 K. It is observed that the defect-free continuous smooth film surface of the as-deposited sample (Fig. 3a) progressively breaks up into individual particles (Fig. 3k) as the annealing temperature is increased. No ordering is observed in this discontinuous particle network. This change of the surface morphology of the film is accompanied by variations in the distribution of Co and Cu starting from 873 K, as can be observed in the SEM-EDS elemental mapping shown in Fig. 3h. In this figure, regions appearing red in the micrograph represent the Cu phase, regions appearing blue correspond to the Co phase. The conclusion here is that the homogeneous solid solution of as-deposited film is metastable and first decomposes into two phases during the annealing treatment. It has been reported that a spinodal decomposition process of Cu-Co supersaturated solid solutions occurs after annealing in this temperature range [26]. Although some morphological variations on the surface of the films are easily detected in the SEM micrographs of the samples annealed for 4 h at 673 and 773 K (Fig. 3c and e), changes on the elemental distribution of both Co and Cu cannot be resolved in the SEM-EDS elemental mapping of Fig. 3d and f. Co rich regions can be clearly observed by SEM-EDS elemental mapping in samples annealed at temperatures above 873 K due to coarsening by Ostwald ripening [37] after spinodal decomposition. This process will be further discussed in details.

Cu and Co agglomerates sparsely distributed on the sapphire substrates begin to be detected in the SE-SEM images recorded at low magnifications for annealing temperatures higher than 973 K (see supplementary material Fig. S1). Finally, isolated and dewetted particles of almost spherical shape with sizes ranging from hundreds of nanometers to several microns can be observed in Fig. 3k on the sapphire substrate in the samples annealed for 4 h at 1073 K. Since the solubility of Co in Cu is less than ∼ 2 at. % at 1073 K [20], SEM-EDS maps (Fig. 3l) show that Co is practically absent from the coarser particles, but is gathered in the shape of isolated particles of about 100 nm in contact with the Cu particles.

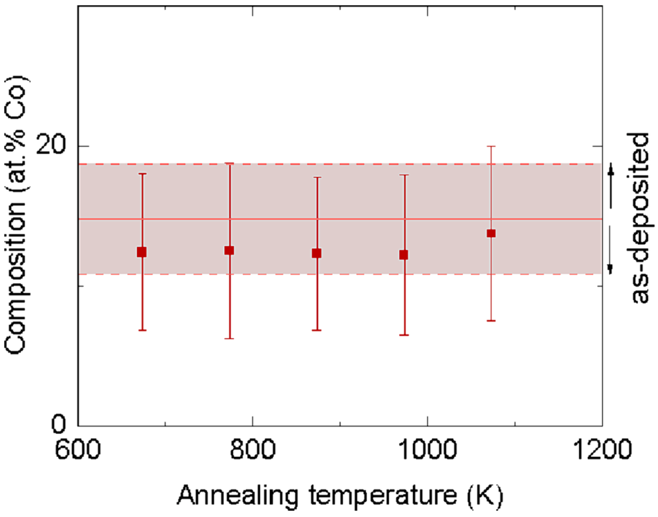

Fig. 2. Average composition determined from SEM-EDS spectra of the films in the as-deposited (pink shaded region) and post-annealed states (red squares). (For interpretation of the references to color in this figure legend, the reader is referred to the web version of this article.)

XRD patterns recoded in the 2θ range between 10° to 100° on the sample in the as-deposited state and after annealing at 673, 873 and 1073 K are shown in Fig. 4. The evolution of the most intense peaks with increasing the annealing temperature can be clearly followed in Fig. 4b and c, which corresponds to zoomed regions of these Bragg reflections. It can be observed in Fig. 4b that only the diffraction peaks of a unique FCC phase are present for the as-deposited film, which agrees with the good mixing of Co and Cu atoms observed in SEM-EDS and TEM-EDS elemental mapping. With the configuration used for XRD measurements, only the lattice planes lying parallel to the film surface contribute to the recorded patterns. The fact that only {1 1 1} and {2 2 2} reflections are strong while the others are absent or have a very weak intensity in the diffraction patterns reveals that the film in all conditions (as-deposited and annealed at 673, 873 and 1073 K) has a strong {1 1 1}

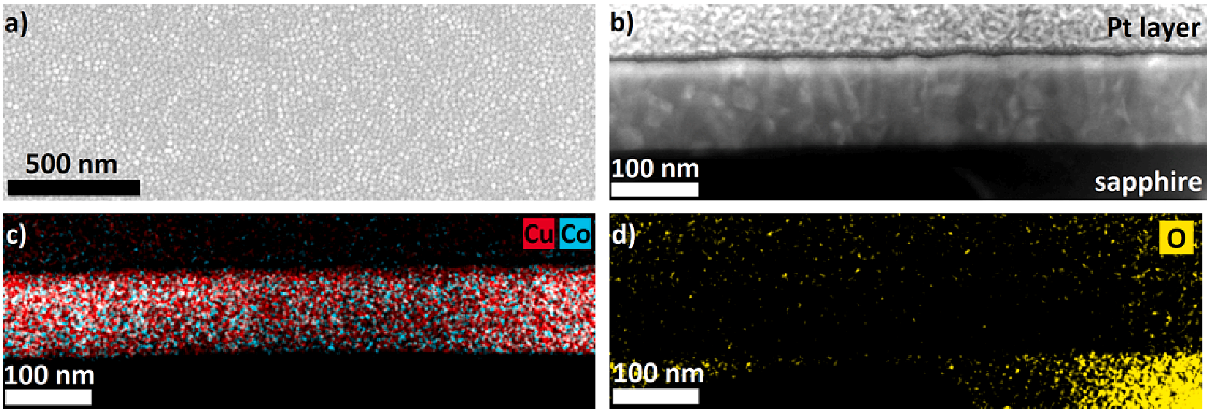

Fig. 1. a) SE-SEM plane view of the as-deposited film, b) ADF cross section image of the as-deposited film, c) elemental distribution at the cross-section of the film obtained from the TEM-EDS of c) Co and Cu and d) O. The gradient in the signal density of Co and Cu in (c) and O (from sapphire) in (d) is due to the gradient of the lamella thickness.

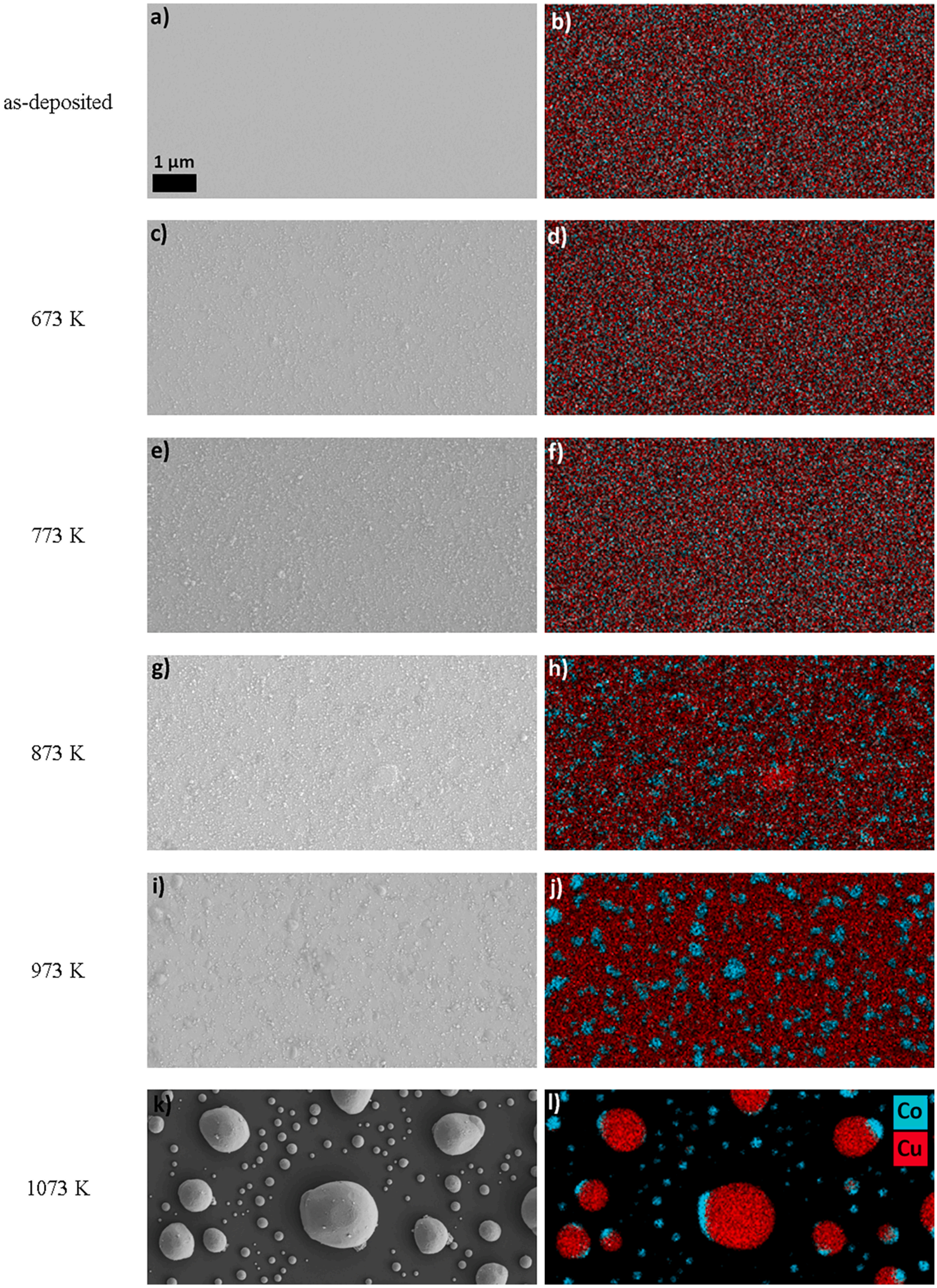

Fig. 3. SE-SEM plane view images (all at the same magnification) of the films in the as-deposited and post-annealed states and their corresponding SEM-EDS maps. Color code: red is Cu and blue is Co. (For interpretation of the references to color in this figure legend, the reader is referred to the web version of this article.)

crystallographic texture. Additionally, {1 1 1} pole figure measurements indicate that the film, even in as-deposited state, has a preferred orientation relationship (OR) with the sapphire substrate (CoCu film $(111)[1\bar{1}0]\|$ Al_2O_3 $(0001)[10\bar{1}0]$, see supplementary material Fig. S2), although many fine grains are visible in the TEM cross-section of the film (Fig. 1b).

The positions of {1 1 1} and {2 2 2} peaks are closer to the vertical solid line corresponding to the position of pure Cu peaks than to the position of pure Co, as expected from Vegard’s law for a binary Cu-Co solid solution with low alloying concentrations of Co. Thus, the lattice parameter determined using the Rietveld refinement (Fig. 4d) is about $\sim$ 0.36 % lower than that of pure Cu when $\sim$ 15 at. % Co is in solid solution.

Fig. 4b and c show broadening of Cu diffraction peaks in the sample annealed at 673 K for 4 h that were found to be asymmetric in nature. Peak profile analysis by Rietveld refinement showed that line

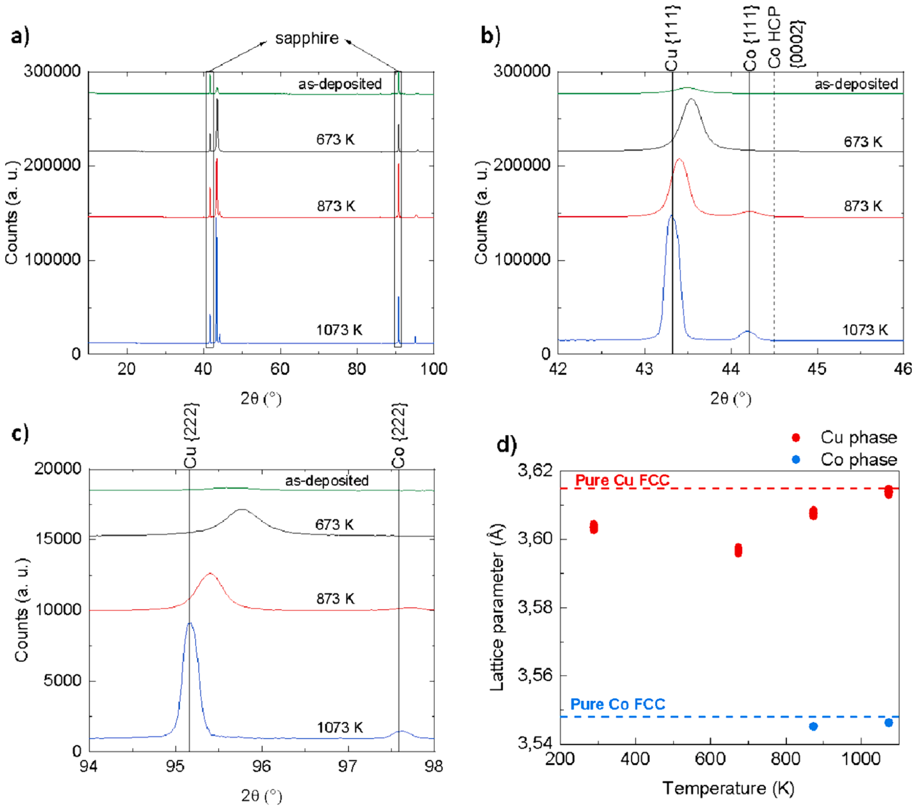

Fig. 4. a) XRD patterns of the film in the as-deposited state and after annealing at 673, 873 and 1073 K for 4 h including sapphire substrate peaks marked by rectangles; detailed evolution of b) {111} and c) {222} Cu (FCC) and Co (FCC) phase reflections and d) lattice parameter of each phase determined using the Rietveld refinement.

broadening cannot be associated to micro-strain and/or crystallite size contributions. In this case, composition fluctuation around the as-deposited composition would cause splitting of the diffraction peaks, which will be masked by the lines' broadening. Thus, significantly anisotropic peaks of a unique FCC phase will be observed in the diffraction pattern. It was concluded that significant compositional heterogeneity due to some phase separation must occur during annealing at 673 K, which was related with the spinodal decomposition process of the Cu-Co super-saturated solid solutions reported previously. Despite these observations justifying Co separation from Cu, the Cu lattice parameter determined using the Rietveld refinement (Fig. 4d) is about ~ 0.20 % lower than the lattice parameter in the as-deposited state. This point will be discussed later.

After annealing at 873 K the XRD patterns shown in Fig. 4b and c exhibited a minor Co phase fraction besides the Cu phase reflections. Only the {111} and {222} Co peaks appeared in the diffraction patterns. Furthermore, the position of the Cu reflections was shifted to lower angles, which implies an increase in the lattice parameter of this phase (by ~ 0.17 %) as shown in Fig. 4d. These observations agree with SEM-EDS observations of Fig. 3h showing that when the sample is annealed at higher temperatures (873 K), phase separation accelerates.

The evolution of the lattice parameter of the two phases with increasing annealing temperature observed in Fig. 4d show that the Cu phase still contains some Co solutes after annealing at 873 K since its lattice parameter is smaller than that of pure Cu (3.615 nm) [27]. However, the Co-rich phase formed from the metastable Cu-Co solid solution do not contain a detectable amount of Cu and the lattice parameters shown in Fig. 4d is similar to the pure Co FCC (3.548 nm) [27].

Finally, at 1073 K the phase separation is complete as the 2θ position of the {111} and {222} peaks of both FCC Cu and FCC Co phases i.e. their lattice parameters match with those of pure FCC Cu and FCC Co (Fig. 4b, c and d). Another conclusion from this observation is that the system has reached a thermally stable state and peak broadening analysis of the diffraction peaks shows no contribution associated with either micro-strain and or crystallite size.

TEM cross-sectional ADF images of the films annealed at 673, 873 and 1073 K along with their corresponding TEM-EDS composition maps are shown in Figs. 5, 6 and 7. The microstructure of nano-sized grains shown in Fig. 1b for the as-deposited films coarsens during annealing at 673 K causing a decrease of the height to diameter ratio, as observed in Fig. 5a. On the other hand, TEM-EDS mapping presented in Fig. 5b shows phase separation due to spinodal decomposition during annealing that gives rise to Co-rich precipitates at the grain boundaries as well as inside the grains. The lack of diffraction peaks of this phase in the XRD pattern of Fig. 4b and c can be due to the small size of the crystallite resulting from a very limited growth rate at this annealing temperature. Since the crystallite size observed in Fig. 5b is about several tens of nanometers, severe peak broadening will produce a peak height lower than the limit of detection. Finally, the elemental distribution map of oxygen in Fig. 5c displays the presence of some oxides at the surface of the film formed during annealing.

Fig. 6 shows that the size of Co clusters has increased by an order of magnitude for the sample annealed at 873 K due to coarsening by Ostwald ripening [37] after spinodal decomposition. This figure also shows copper rich grains with hillock shape, which was also observed previously in the plane-view SEM images of Fig. 3g.

Finally, in Fig. 7, the formation of dewetted and isolated particles consisting of (almost) pure Cu and Co after annealing at 1073 K is observed (as it was also observed in SEM-EDS maps in Fig. 3l). This figure shows two connected Cu-rich and Co-rich particles, both with faceted morphology which include recrystallized twins inside (shown by white arrows in Fig. 7a). In addition, very small Co-rich regions confined to the initial film thickness are observed in the corresponding TEM-EDS map (shown by arrows in Fig. 7b). Similar small Co-rich particles,

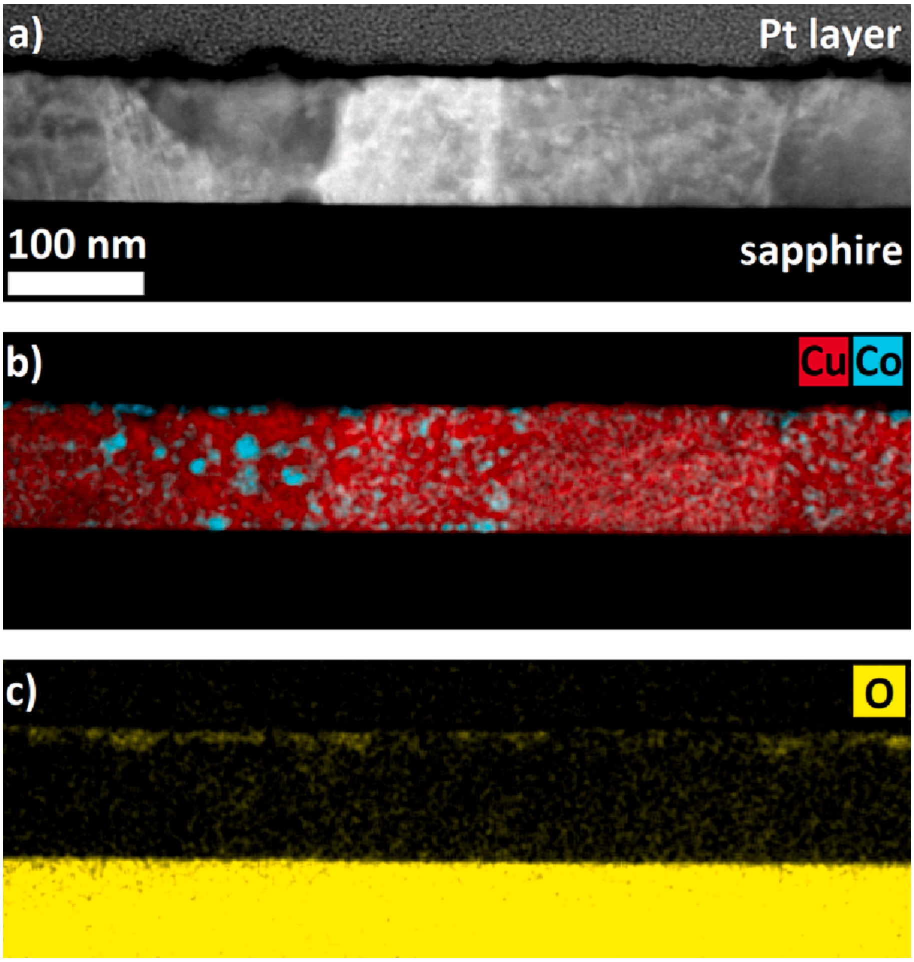

Fig. 5. TEM microstructural analysis of a film annealed at 673 K for 4 h: a) ADF cross section image and corresponding elemental distribution obtained from EDS spectrum of b) Co and Cu and c) O, which was related with the formation of oxides at the surface.

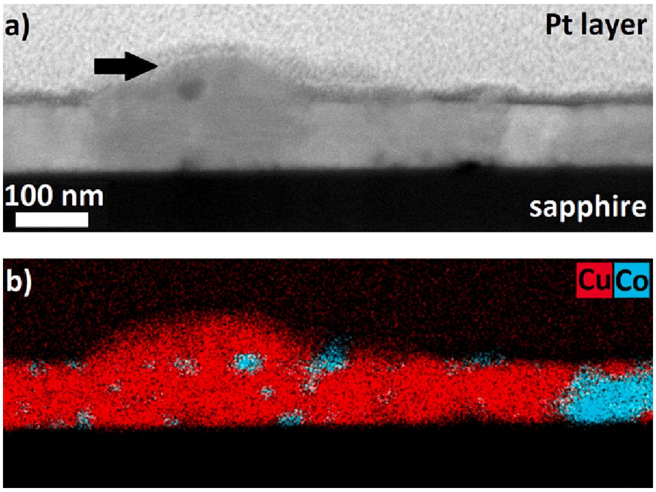

Fig. 6. TEM microstructural analysis of a film annealed at 873 K for 4 h: a) ADF cross section image including black arrow to highlight Cu-rich hillock and b) corresponding elemental distribution of Co and Cu obtained from EDS spectrum.

however isolated, are also observed in the SEM-EDS of this experiment (Fig. 3l).

Grain size evolution determined from TEM cross-sectional images as a function of the annealing temperature is plotted in Fig. 8. This figure shows that the average columnar grain size has increased from 25 nm for as-deposited film to over 75 and 125 nm for the films annealed at 673 and 873 K, respectively.

4. Discussion

In this section, we address three mechanisms which have mainly affected the microstructural evolution of our CoCu solid-solution film observed in the previous section.

1. Grain growth and groove formation

As Mullins [28] had pointed out, grooving is one of the mechanisms which prevents grain growth in thin films. Grooves form at energetically favorable locations such as dislocations, high energy grain boundaries and triple junctions. These grooves transform into holes and cause film rupture by deepening with time and expanding across the entire film thickness. When we formulate the groove depth in terms of the film thickness and grain size [9,15], a critical value for the grain size, R_c, is obtained:

$$R_c = \frac{3\sin^3\theta}{2 - 3\cos\theta + \cos^3\theta}t, \qquad with \;\; \theta = \sin^{-1}(\gamma_G/2\gamma_\nu) \tag{1}$$

γ_G and γ_ν are the grain boundary and film surface energy, respectively, θ is the equilibrium angle at which the film surface intersects the grain boundary and t is the film thickness. If during the annealing process and growth of the grains, the size of the grains reaches this value, grooving is expected to happen in the film. These grooves stop grain growth and the grain size stagnates at R_c. If the grain size stagnates below R_c before the

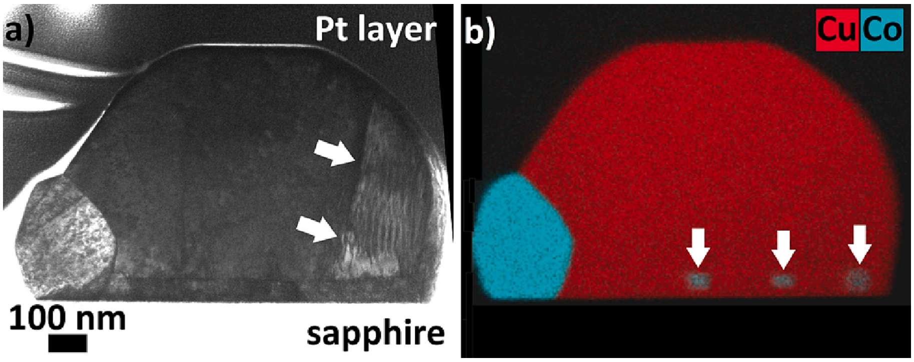

Fig. 7. TEM cross section from an isolated particle in a sample annealed at 1073 K for 4 h: a) bright field (BF) image where the white arrows indicate a twin boundary and b) corresponding elemental distribution of Co and Cu obtained from TEM-EDS. The white arrows indicate small Co-rich regions.

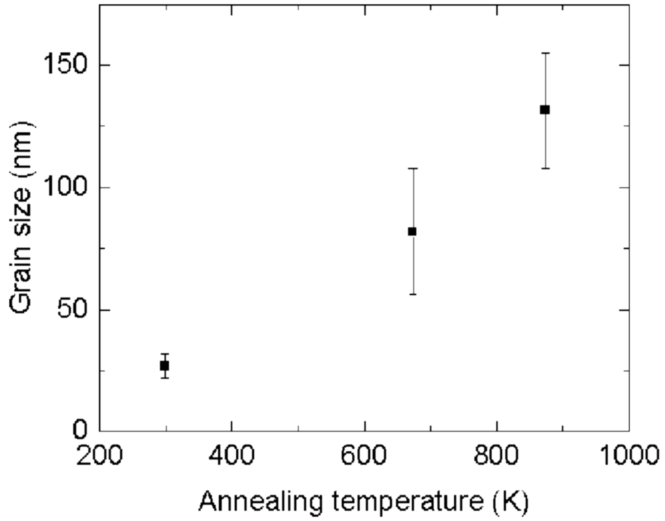

Fig. 8. Evolution of grain size as a function of the annealing temperature. The error bars included in the figure correspond to the standard deviation calculated from 10 measurements.

end of the annealing process (when there is a force against grain growth such as Zener drag), then it is not expected that the film dewets through groove deepening [9]. Using the surface and grain boundary energy of pure Cu at 773 K (1361 & 668 mJ/m^2, respectively) [17] we calculated R_c, considering that the alloy consists mainly of Cu (~85 at. %). These calculations show that R_c is almost 14 times the film thickness, which is ~ 1400 nm for our film. However, when the films were annealed at 673 K and 873 K, it is observed that the average grain size is much smaller (below 150 nm) than R_c (Fig. 8).

It has been reported that, in isothermal experiments, grain growth and texture evolution occur mostly at the beginning of the annealing and longer annealing time does not dramatically affect the grain size anymore [29]. This observation means that the grain size that has been reached in our system was already stagnating before the end of the ~ 4 h annealing duration. This suggests that some dragging force hinders further grain growth. According to Refs. [30,31] precipitates forming at grain boundaries can hinder grain growth by exerting the so called "Zener drag" on grain boundary motion. TEM-EDS cross-section of the film at 673 K (Fig. 5b) actually shows the formation of Co precipitates at grain boundaries and interfaces. These precipitates have formed as a result of annealing and alloy demixing since it is shown by XRD (Fig. 4b, c) and cross sectional TEM-EDS (Fig. 1c) that the as-deposited film had a homogeneous solid solution structure.

2. Phase separation

Considering the relatively small mixing enthalpy of Co and Cu, of the order of 20 kJ/mole [32], phase separation occurred at the beginning of the isothermal annealing experiments, resulting in the formation of Co precipitates. The diffusion length of Co atoms after 4 h of annealing at 673 K can be calculated via the following equation:

$$x = \sqrt{2Dt} \tag{2}$$

x Is the diffusion length, D is the diffusion constant at 673 K and t is the annealing duration. Using the diffusion constant of Co in Cu reported in Ref. [33] (1.58 10^{-17} cm^2/s at 680 K) the diffusion length is ~ 6.7 nm. This value shows that Co atoms are not very mobile at this temperature. Moreover, Co content is much smaller compared to Cu in the system. These simple estimations can explain why many small dispersed Co precipitates have formed locally within the Cu grains and some larger at energetically favourable sites i.e. Interfaces and grain boundaries. However, the size and volume fraction of these precipitates are not large enough so that an XRD diffraction peak for Co phase, comparable in height with other intense peaks, could be observed (Fig. 4b, c). Instead, this phase separation represented itself as line broadening (after Rietveld refinement) in Cu diffraction peaks which could not be associated with micro-strain or crystallite size, as mentioned in the previous section. In addition to the above mentioned so-called "binodal" decomposition, spinodal decomposition might have occurred simultaneously. The decomposition process in this case is driven by diffusion as well. In previous studies, spinodal decomposition in CoCu alloy with 10 at. % Co has been observed in coexistence with binodal decomposition at 703 K [34]. Considering the free energy of the CoCu system [35]

$$G_c = \left[\sum_j \Omega_j(T) c^j\right] c^2 + RT[c\ln(c) + (1-c)\ln(1-c)] \tag{3}$$

$$\Omega_0(T) = -60225 + 16.226T\left(\frac{J}{mol}\right)$$

$$\Omega_1(T) = 7150 - 1.9376T\left(\frac{J}{mol}\right)$$

$$\Omega_j(T) = 0, \qquad j \geq 2$$

for spinodal decomposition we should have:

$$\frac{\partial G_c^2}{\partial c^2} < 0 \tag{4}$$

G_c and T represent the free energy at composition c (in Co) and temperature , respectively. In our case where c $\sim 15 at.\%$, the spinodal decomposition is expected below 1200 K. In any case, the Co precipitates are energetically favoured to nucleate at grain boundaries and interfaces.

Although we did not observe the initiation of dewetting in the alloyed CuCo film at 673 K, Derkach *et al.* [14] have observed hole formation in a pure Cu film of similar thickness already at 573 K after annealing for 30 min. Additionally, Sonawane and Kumar [36] have observed complete agglomeration of a 100 nm thick Cu film into particles and islands after annealing at 873 K for 2 h. From what has been discussed earlier, we can conclude that the formation of Co precipitates at the grain boundaries in the CoCu film activates the Zener drag force and causes the stagnation of grain size below R_c. As a result, the film does not dewet at the mentioned temperatures (673 and 873 K) by the grooving mechanism.

A larger volume content of Co-rich regions can be observed at 873 K (Fig. 6b) and 1073 K (Fig. 7b) when compared to 673 K (Fig. 5b), and therefore they are clearly resolved by XRD (Fig. 4b, c). This observation can be explained in terms of Ostwald ripening [37]. Diffusion becomes faster by increasing temperature, which leads to larger Co-rich particles. On the other hand, some small clusters were still observed, especially at 1073 K, either confined to the initial film thickness (Fig. 7b) or turned to individual Co-rich particles dispersed on the substrate (SEM-EDS of 1073 K, Fig. 3). Co atoms should first overcome the positive mixing enthalpy with Cu [32] and diffuse out of clusters, in order to join other Co atoms and form larger clusters/particles. This process makes the energy barrier larger for Co diffusion and the mobility of Co becomes smaller compared to Cu self-diffusion. As a result, some Co clusters join together to build larger Co-rich particles whereas some others stayed in place. On the other hand, according to Fig. 4d the Cu matrix contains a small amount of Co solutes at temperatures lower than 1073 K. By annealing the CoCu film at 1073 K, the remaining Co separates from the Cu matrix and forms the small Co clusters.

The larger Co-rich particles are almost Co pure as no large shift is observed in the Co {1 1 1} peak between 873 K and 1073 K (Fig. 4b), and the solubility of Cu in Co is very low at these temperatures ($<$2 at. %) [20]. Moreover, these particles adopt an FCC structure, in agreement with the phase diagram of CoCu [20], where Co has a FCC structure at temperatures of 873 and 1073 K. Through the relatively fast cooling process after each heat treatment, Co maintained an FCC structure and did not reach its equilibrium structure (HCP) at lower temperatures as previously observed also in literature for pure Co thin films [38]. On the other hand, Co particles maintained the symmetry of their Cu-rich matrix, leading to adoption of the same phase of Cu FCC at a low energy cost since the stacking fault energy which allows to switch from HCP to FCC is low.

As mentioned earlier, the lattice parameter of the Co-rich and Cu-rich phases at 1073 K coincides with those of the pure Cu FCC and Co FCC. Since the lattice parameters are not affected by a slight solid solution effect, then it can be concluded that there is no noticeable stress in the film. However, such conclusions does not apply to the films in the as-deposited state and those annealed at 673 and 873 K. Despite of this, we can still address stress relaxation mechanisms and their representation in our films.

3. Stress.

The as-deposited film is under compressive stress indicated by wafer curvature measurements (see supplementary material Fig. S3), as expected from the deposition method via sputtering. By annealing this stress is partly relaxed from the film. This relaxation corresponds to a decrease in the lattice parameter of the film annealed at 673 K (Fig. 4d).

On the other hand, thin films undergo thermal stresses at higher temperatures. Thermal stress can be tensile or compressive depending on the difference of the thermal expansion coefficients between the substrate and the film. In the case of pure Cu films on (0001) Al_2O_3 this stress is compressive during heating and tensile while cooling [39]. We make a similar assumption for our alloy containing Cu in majority. Furthermore, a polycrystalline structure and presence of grain boundaries puts additional constraints on the film. Compressive stress relaxation occurs via a mix of dislocation plasticity, twinning and diffusional creep [40]. Twins and dislocations that were observed in the film after annealing e.g. at 1073 K (Fig. 7a) are the signature of such phenomena. Besides, diffusional creep can lead to grain boundary motion and grain growth [41] which was also observed in Fig. 8 for the film annealed at 673 K. Hillock formation is another consequence of diffusional creep. Normally, in the absence of a passivation layer, surface diffusion occurs prior to grain boundary and bulk diffusion due to the smaller activation energy [42]. When there exists a passivation layer at the surface, the surface diffusion is suppressed and grain boundary diffusion becomes a dominant mechanism for atomic diffusion.

In the CoCu films of this study grain growth was stagnating at early stages due to the formation of Co precipitates at grain boundaries (as discussed earlier), which in turn prevent further stress relaxation through grain boundary motion. Moreover, the formation of Co precipitates at the film surface as well as the presence of an oxide layer, clearly observed at 673 K (Fig. 5c), suppressed the surface diffusion. Therefore, the stress must have been released through other mechanisms such as hillock formation (Fig. 6). The hillocks, which have formed at 873 K, mostly consisted of Cu because of the smaller diffusivity of Co compared to Cu as discussed earlier.

5. Summary and conclusion

In this study, we investigated the effect of Co in a super-saturated CuCo alloy thin film on the microstructure evolution and solid-state dewetting behavior. Super-saturated CoCu solid solution films of 15 at. % Co were produced by sputtering and heat treated at different temperatures. We observed the hole formation and dewetting within the CoCu film occurring at a higher temperature compared to pure Cu films. The temperature delay in dewetting is mainly caused by the formation of Co precipitates at grain boundaries and interfaces as a result of a spinodal-type decomposition occurring at relatively low temperatures of 673 K. Co precipitates at the grain boundaries hinder the grain growth and as a result, the critical grain size (*Rc*) for initiation of grooving was not reached in the alloyed film. Moreover, these precipitates at the interfaces also slow down the diffusion of Cu atoms.

According to our observations, the following stages are proposed for achieving dewetting of CuCo films:

- Phase separation occurs prior to completion of grain growth. As a result, Co precipitates form at grain boundaries, applying Zener drag forces, which stagnate the grain size below a critical value R_c at which grooving is expected.
- Ostwald ripening of Co precipitates leads to coarsening especially for precipitates at the grain boundaries. Thus, Zener drag preventing grain growths diminishes.
- Finally, grain growth and grooving occur creating holes in the film. Through diffusional processes these holes grow and the film dewets. Simultaneously, the phase separation process continues until decomposition reaches thermodynamic equilibrium.

The study provides fundamental concepts, which can be employed to enhance the stability of structural and functional metallic films exposed to high temperatures.

Research Data.

The data that support the findings of this study are available from the corresponding author upon reasonable request.

CRediT authorship contribution statement

Farnaz Farzam: Writing – original draft, Visualization, Validation, Investigation, Data curation. **Bárbara Bellón:** Writing – review & editing, Validation, Supervision, Formal analysis. **Dominique Chatain:** Writing – review & editing, Validation, Methodology. **José A. Jiménez:** Formal analysis, Investigation, Writing – review & editing. **Benjamin Breitbach:** Writing – review & editing, Investigation, Formal analysis. **Matteo Ghidelli:** Writing – review & editing, Validation, Supervision. **María Jazmin Duarte:** Writing – review & editing, Validation, Supervision. **Gerhard Dehm:** Writing – review & editing, Validation, Supervision, Funding acquisition, Conceptualization.

Declaration of competing interest

The authors declare the following financial interests/personal relationships which may be considered as potential competing interests: Gerhard Dehm reports financial support was provided by European Research Council. Maria Jazmin Duarte reports financial support was provided by European Research Council. Dominique Chatain reports financial support was provided by Alexander von Humboldt Foundation. If there are other authors, they declare that they have no known competing financial interests or personal relationships that could have appeared to influence the work reported in this paper.

Data availability

Data will be made available on request.

Acknowledgments

DC is grateful for financial support by the Alexander von Humboldt foundation. GD and MJD acknowledge financial support by the European Research Council (ERC) under the EU's Horizon 2020 Research and Innovation Program (ERC Advanced Grant, GB-Correlate, Grant No. 787446).

Appendix A. Supplementary data

Supplementary data to this article can be found online at https://doi.org/10.1016/j.matdes.2024.112892.

References

[1] S. Kim, C. Shim, J. Hong, H. Lee, J. Han, K. Kim, Y. Kim, Copper hillock induced copper diffusion and corrosion behavior in a dual damascene process, Electrochem. Solid St. 10 (6) (2007) H193–H195.
[2] C. Fei, W. Gao-hui, J. Long-tao, C. Guo-qin, Feasibility study on the use of Cu (Co) alloy for barrierless copper metallization, Thin Solid Films 599 (2016) 31–36.
[3] G. Dehm, T. J. Balk, H. Edongué, E. Arzt "Small-scale plasticity in thin Cu and Al films" Microelectronic Engineering, 70 (2-4) (2003), pp. 412-424.
[4] R. P. Vinci, E. M. Zielinski, J. C. Bravman "Thermal strain and stress in copper thin films" Thin solid films, 262 (1-2) (1995), pp. 142-153.
[5] J.R. Lloyd, J. Clemens, R.J.M.R. Snede, Copper metallization reliability, Microelectron. Reliab. 39 (11) (1999) 1595–1602.
[6] W.B. Pennebaker, Hillock growth and stress relief in sputtered Au films, J. Appl. Phys. 40 (1) (1969) 394–400.
[7] H. Esch, G. Huyberechts, R. Mertens, G. Maes, J. Manca, W. De Ceuninck, L. De Schepper "The stability of Pt heater and temperature sensing elements for silicon integrated tin oxide gas sensors" Sensors and Actuators B: Chemical, 65 (1-3) (2000), pp. 190-192.
[8] S. Liou, C.L. Chien, Granular metal films as recording media, Appl. Phys. Lett. 52 (6) (1988) 512–514.
[9] C.V. Thompson, Solid-state dewetting of thin films, Annu. Rev. Mat. Res. 42 (2012) 399–434.
[10] E. Jiran, C.V. Thompson, Capillary instabilities in thin films, J. Electron. Mater. 19 (1990) 1153–1160.
[11] E. Jiran, C.V. Thompson, Capillary instabilities in thin, continuous films, Thin Solid Films 208 (1) (1992) 23–28.
[12] D.J. Srolovitz, M.G. Goldiner, The thermodynamics and kinetics of film agglomeration, JOM 47 (1995) 31–36.
[13] D. Chatain, B. Courtois, I. Ozerov, N. Bozzolo, M. Kelly, G.S. Rohrer, P. Wynblatt, Growth and orientation relationships of Ni and Cu films annealed on slightly miscut (11 02) r-sapphire substrates, J. Cryst. Growth 508 (2019) 24–33.
[14] V. Derkach, A. Novick-Cohen, A. Vilenkin, E. Rabkin, Grain boundary migration and grooving in thin 3-D systems, Acta Mater. 65 (2014) 194–206.
[15] D.J. Srolovitz, S.A. Safran, Capillary instabilities in thin films. I. Energetics, J. Appl. Phys. 60 (1) (1986) 247–254.
[16] A. Kosinova, O. Kovalenko, L. Klinger, E. Rabkin, Mechanisms of solid-state dewetting of thin Au films in different annealing atmospheres, Acta Mater. 83 (2015) 91–101.
[17] J.Y. Kwon, T.S. Yoon, K.B. Kim, S.H. Min, Comparison of the agglomeration behavior of Au and Cu films sputter deposited on silicon dioxide, J. Appl. Phys. 93 (6) (2003) 3270–3278.
[18] Y. Minamide, M. Kawamura, Y. Abe, K. Sasaki, Agglomeration suppression behavior and mechanisms of Ag–Cu and Ag–Nb thin films, Vacuum 84 (5) (2009) 657–662.
[19] C. Manuela Müller, R. Spolenak, Dewetting of Au and AuPt alloy films: a dewetting zone model, J. Appl. Phys. 113 (9) (2013).
[20] T. Nishizawa, K. Ishida, The Co-Cu (Cobalt-Copper) System, Bull. Alloy Phase Diagr. 2 (1984) 161–165.
[21] J.R. Childress, C.L. Chien, Reentrant magnetic behavior in fcc Co-Cu alloys, Phys. Rev. B 43 (10) (1991) 8089.
[22] A.M. Mebed, J.M. Howe, Spinodal induced homogeneous nanostructures in magnetoresistive CoCu granular thin films, J. Appl. Phys. 100 (7) (2006).
[23] A. Hütten, G. Thomas, "Investigation of heterogeneous $Cu_{1-x}Co_x$ alloys with giant magnetoresistance", Ultramicroscopy, 52 (3-4) (1993), pp. 581-590.
[24] A.M. Mebed, Microstructure evolution, film rupture and the existence of metastable phases in CoCu films, Physica Status Solidi (a) 201 (1) (2004) 11–16.
[25] R. E. Dinnebier, A. Leineweber, J. S. Evans, "Rietveld refinement: practical powder diffraction pattern analysis using TOPAS", Walter de Gruyter GmbH & Co KG, (2018).
[26] M.G.M. Miranda, E. Estévez-Rams, G. Martinez, M.N. Baibich, Phase separation in $Cu_{90}Co_{10}$ high-magnetoresistance materials, Phys. Rev. B 68 (1) (2003) 014434.
[27] A.V. Chichagov, Information-calculating system on crystal structure data of minerals (MINCRYST), Mater. Sci. Forum (1994) 193–198.
[28] W.W. Mullins, Theory of thermal grooving, J. Appl. Phys. 28 (3) (1957) 333–339.
[29] F. Niekiel, S.M. Kraschewski, P. Schweizer, B. Butz, E. Spiecker, Texture evolution and microstructural changes during solid-state dewetting: A correlative study by complementary in situ TEM techniques, Acta Mater. 115 (2016) 230–241.
[30] C.S. Smith, Grains, phases, and interfaces: An introduction of microstructure, Trans. Metall. Soc. AIME 175 (1948) 15–51.
[31] D.J. Srolovitz, M.P. Anderson, G.S. Grest, P.S. Sahni, Computer simulation of grain growth-III. Influence of a particle dispersion, Acta Metall. 32 (9) (1984) 1429–1438.
[32] M.A. Turchanin, P.G. Agraval, Phase equilibria and thermodynamics of binary copper systems with 3 d-metals. V. Copper-cobalt system, Powder Metall. Met. Ceram. 46 (2007) 77–89.
[33] R. Döhl, M.P. Macht, V. Naundorf, Measurement of the diffusion coefficient of cobalt in copper, Physica Status Solidi (a) 86 (2) (1984) 603–612.
[34] R. Busch, F. Gärtner, C. Borchers, P. Haasen, R. Bormann, High resolution microstructure analysis of the decomposition of $Cu_{90}Co_{10}$ alloys, Acta Mater. 44 (6) (1996) 2567–2579.
[35] A.M. Mebed, M.I. Abd-Elrahman, A.M. Abd-Elnaiem, M.A. Gaffar, Thermal analysis study for the phase determination and instable to metastable transformation of the Co–13Cu alloy, Phase Transit. 82 (8) (2009) 587–598.
[36] D. Sonawane, P. Kumar, Stability of Cu-islands formed on Si substrate via 'dewetting' under subsequent thermal cycling, Nanotechnology 32 (19) (2021) 195703.
[37] R.A. Oriani, Ostwald ripening of precipitates in solid matrices, Acta Metall. 12 (12) (1964) 1399–1409.
[38] V.M. Marx, C. Kirchlechner, B. Breitbach, M.J. Cordill, D.M. Többens, T. Waitz, G. Dehm, Strain-induced phase transformation of a thin Co film on flexible substrates, Acta Mater. 121 (2016) 227–233.
[39] G. Dehm, T. J. Balk, H. Edongué, E. Arzt, "Small-scale plasticity in thin Cu and Al films", Microelectronic Engineering, 70 (2-4) (2003), pp. 412-424.
[40] P. Chaudhari, Hillock growth in thin films, J. Appl. Phys. 45 (10) (1974) 4339–4346.
[41] P. Chaudhari, Grain growth and stress relief in thin films, J. Vac. Sci. Technol. 9 (1) (1972) 520–522.
[42] M. Ohring, S. Zarrabian, A. Grogan, The materials science of thin films, Appl. Opt. 31 (34) (1992) 7162.